**This paper must be cited as:**
Carneiro, A. N., Mamontova, E., Botas, A. M. P., Brites, C. D. S., Ferreira, R. A. S., Rouquette, J., Guari, Y., Larionova, J., Long, J., Carlos, L. D., Rationalizing the Thermal Response of Dual-Center Molecular Thermometers: The Example of an Eu/Tb Coordination Complex, 10, 2101870, Advanced Optical Materials (2022)
https://doi.org/10.1002/adom.202101870

# Rationalizing the thermal response of dual-center molecular thermometers: the example of an Eu/Tb coordination complex

*Albano N. Carneiro Neto,† Ekaterina Mamontova,† Alexandre M. P. Botas, Carlos D. S. Brites Rute A. S. Ferreira, Jérôme Rouquette, Yannick Guari, Joulia Larionova, Jérôme Long,* and Luís D. Carlos**

Dr. A. N. Carneiro Neto, Dr. A. M. P. Botas, Prof. C. D. S. Brites, Prof. R. A. S. Ferreira, Prof. L. D. Carlos
Phantom-g, CICECO–Aveiro Institute of Materials, Physics Department, University of Aveiro, 3810-193, Aveiro, Portugal
E-mail: lcarlos@ua.pt

Dr. E. Mamontova, Dr. J. Rouquette, Dr. Yannick Guari, Prof. J. Larionova, Dr. J. Long
ICGM, Univ. Montpellier, CNRS, ENSCM, Montpellier, France
E-mail : jerome.long@umontpellier.fr

**Keywords:** lanthanide coordination complexes, luminescence, molecular thermometers.

Luminescence thermometry allows the remote monitoring of the temperature and holds the promise to drive the next generation of future nano or micrometric devices. Materials able to sense the temperatures are usually based on one or several lanthanide ions allowing a ratiometric measurement. Optimizing the thermometric features is usually achieved through a serendipity approach, but it still appears difficult to accurately predict the sensing performance. Through a combination of experiment and theoretical calculations, we report the first example of an energy-driven luminescent molecular thermometer $[Tb_{0.94}Eu_{0.06}(bpy)_2(NO_3)_3]$ (bpy = 2,2′-bipydine) displaying an exceptional thermal cyclability around room temperature and for which the thermal properties could be theoretically forecasted. This work provides comprehensive guidelines that can be easily extended for any dual-center thermometer in which energy transfer drives the thermometric performance opening the avenue for the smart engineering of sensing devices.

## 1. 1. Introduction

Our days, luminescence thermometry (also called thermographic phosphor thermometry) is in the spotlight of materials science and engineering research representing around 5% of all the papers listed in the principal collection of the Web of Science from Clarivate Analytics with the words luminescence or luminescent in the abstract.[1] The main reason behind the impressive blow-up that occurred in the middle of the last decade[2] was the popularization of light-emitting micro and nanomaterials allowing noninvasive (or, to be precise, semi-invasive) temperature sensing at scales below 1 micron, where the traditional thermometers (*e.g.*, thermocouples and pyrometers) are generally unsuitable.[3-7] The impact of luminescence thermometry has been felt, therefore, in disparate areas, such as biomedicine [8-10] (including *in vivo*[11, 12] and *in vitro*[13, 14] sensing), catalysis,[15, 16] microelectronics,[17-19] Internet of Things,[20] magnetism,[21-24] vacuum sensing,[25] and microfluidics.[26] Indeed, thermographic phosphor thermometry was compared with radiation and contact thermometry in an industrial setting and the results proved that the approach is an effective alternative to conventional techniques offering better performance.[27] Furthermore, in the last couple of years, the technique started to be used as a tool for unveiling properties of the thermometers themselves or of their local surroundings, as, for instance, the estimation of the absorption coefficient and thermal diffusivity of tissues,[28] the determination of the Brownian velocity of colloidal nanocrystals[29] and thermal properties of nanoparticles, including lipid bilayer coatings,[30-32] and the measurement of the phase transition temperature of perovskite oxides.[33]

Among the different proposed methodologies to measure the absolute temperature using light emission, the most popular relies on measuring the intensity ratio of two electronic transitions in thermal equilibrium.[1, 3, 34-37] This popular concept (known as luminescence intensity ratio thermometry, LIR) is described by the simple Boltzmann's law,[38, 39] allowing to overcome some of the limitations affecting the performance of luminescent thermometers based on a single emission.[1, 3, 35] By far, thermometers based on trivalent lanthanide ions ($Ln^{3+}$)[1, 35, 40-44] (including materials co-doped with $Ln^{3+}$ ions and transition metals[45, 46]) have popularized the LIR thermometry concept.

Ratiometric luminescent thermometers can be classified in single-ion (encompassing crossover-[47] and Boltzmann-based systems[39, 45]) and dual-center examples in which energy transfer drives the thermometric performance.[28, 42, 48-52] A theoretical framework for describing ratiometric single-ion Boltzmann-based thermometers was recently established[39] and these systems are one of the very few examples of luminescent primary thermometers,[53] in which the temperature can be predicted without a previous calibration procedure. However, these Boltzmann-based luminescent thermometers are generally ineffective above *ca*. 400 K [38, 39] and their relative thermal sensitivity ($S_r$) rarely exceeds 1%·K$^{-1}$, which can be a constrain in certain applications. $S_r$ is used as a figure of merit to compare the performance of different thermometers[37] since our suggestion in 2012.[3] Thus, dual-center thermometers based on temperature-dependent energy transfer processes are considered the most exciting alternative to circumvent the limitations of single-ion thermometers. However, and despite extensive experimental research in these systems, including the $Tb^{3+}$/$Eu^{3+}$ pair, which is by far the most widely reported, a general theory covering the basics of luminescence thermometry through energy transfer (both in single- and dual-center systems) is nearly nonexistent. There are very few exceptions, such as the $Ho^{3+}$-based thermometer reported by van Swieten *et al.*[52] in which quantitative modeling was presented predicting the output spectrum over a wide range of temperatures (300–873 K) and $Ho^{3+}$ concentrations (0.1–30%), or the series of mixed $Tb^{3+}$/$Eu^{3+}$-codoped metal-organic frameworks (MOFs) reported by Trannoy *et al.* in which a detailed theoretical study on $Tb^{3+}$-to-$Eu^{3+}$ energy transfer processes was performed evidencing a notorious agreement with the experimental data.[51] Yet, optimizing the synthetic design of luminescent thermometers with an improved performance will require not only to post-rationalize the thermometric parameter but, more importantly, to predict it through a concerted theory/experimental approach.

In this sense, lanthanide coordination complexes have recently appeared as a fertile field of research in luminescence thermometry, including the very intriguing example of molecular thermometers displaying single-molecule magnet (SMM) behavior.[21-24] Molecular chemistry concepts could be efficiently used to control the parameters affecting the thermometric parameters by the careful choice of the building blocks (lanthanide ion, ligands, and in turn the intermolecular distances). Yet, one of the general drawbacks of lanthanide molecule-based materials might be associated with their possible lack of thermal stability even in relatively mild conditions (> 50-300° C).[54] This could be mostly related to the presence of interstitial and coordinated solvent molecules, which upon removal might induce a collapse of the crystal structure or a change in the lanthanide's coordination environment that alters the emission features and in turn the overall cyclability in the high-temperature range.[54, 55] This appears particularly relevant for the thermometers based on lanthanide MOFs for which most examples incorporate solvates (coordinated or interstitial) in their frameworks.[41] As an alternative, discrete mono or polynuclear coordination compounds might afford better control over the coordination environment of the lanthanide ion.

Herein, we present the first example in which the thermometric parameter of an energy-driven luminescent thermometer is theoretically predicted showing an astonishing accord with the experimental data. The adopted theoretical methodology is applied to the illustrative example of the $[Tb_{0.94}Eu_{0.06}(bpy)_2(NO_3)_3]$ coordination complex displaying very high thermal sensing reproducibility (>97%). The presented approach can be easily extended for any dual-center thermometer in which energy transfer drives the thermometric performance opening the avenue for the smart engineering of dual-center thermometers instead of the common trial-and-error strategy.

# 2. 2. Results and Discussion

## 2.1. 2.1 Synthesis, crystal structure, and characterization

To demonstrate our approach, we selected a well-known simple lanthanide complex of formula $[Ln(bpy)_2(NO_3)_3]$ (bipy = 2,2'-bipyridine),[56] but for which the thermometric properties were never investigated to our knowledge. This complex presents several advantages such as: *i*) efficient lanthanide sensitization by the bpy ligands;[57] *ii*) chemical stability in the presence of air and water; *iii*) absence of solvent molecules, and i*v*) easy synthesis in large yields and at the multigram scale.

The first syntheses of $[Ln(bpy)_2(NO_3)_3]$ complexes were reported in the 1960s[58-60] and an isostructural series has been obtained over several decades.[56, 61] In our study, the mixed complex was synthesized by adapting the procedures already reported.[60, 62] Hence, the reaction between a 95/5 mixture of $Tb(NO_3)_3{\cdot}6H_2O$ and $Eu(NO_3)_3{\cdot}6H_2O$ with two equivalents of bpy in ethanol affords the formation of single crystals of $[Tb_{0.94}Eu_{0.06}(bpy)_2(NO_3)_3]$ (**1**) in 39 % yield. Interestingly, the compound could be easily obtained in better yield (*i.e.* 82 %) by the fast precipitation of the molecular precursors.

X-ray diffraction analysis on single-crystals indicates that **1** crystallizes in the orthorhombic *Pbcn* space group with half a complex in the asymmetric unit. The compound is isostructural to the previously reported pure terbium and europium analogs.[56, 63] The calculated lanthanide site occupancy of $Tb_{0.95}Eu_{0.05}$ obtained from the structural refinement is in excellent agreement with the Eu/Tb ratio of 6% found by energy-dispersive spectroscopy (EDS) analysis. The coordination sphere of the lanthanide center is constituted by two bpy and three bidentate nitrate moieties giving a coordination number of 10 (Figure 1a). Qualitative analysis of the coordination geometry using the SHAPE software[64] indicates an intermediate geometry between a bicapped square antiprism and a spherocorona (Table S1 in Supporting Information). The Ln-N distances, ranging from 2.525(1) to 2.549(4) Å, are slightly longer than the Ln-O ones involving the nitrate moieties (2.455(1)–2.478(1) Å, Table S2 in Supporting Information). Analysis of the crystal packing reveals the presence of intermolecular $\pi$-stacking interactions between the bpy ligands (Figure 1b), while the shortest Ln-Ln distance is equal to 7.696 Å.

Thermogravimetric analysis confirms the absence of solvent molecules and indicates thermal stability of the complex up to 290°C (Figure S1 in Supporting Information). The powder X-ray diffraction patterns (Figure S2 in Supporting Information), in line with other analyses, confirm the purity of the sample. The magnetic properties were investigated in static and dynamic modes and confirm the expected paramagnetic behavior (Figures S3-S4 in Supporting Information).

## 2.2. 2.2 Photoluminescence

The emission spectra of **1** (12-450 K) reveal the characteristic luminescence of $Tb^{3+}$ and $Eu^{3+}$ ascribed to the $^5D_4 \rightarrow {}^7F_{6-3}$ and $^5D_0 \rightarrow {}^7F_{0-4}$ transitions, respectively (Figure 2a). As the temperature is increased to 450 K, an increase of the relative intensity of the $Eu^{3+}$ intra-$4f^6$ with respect to that of the $Tb^{3+}$ intra-$4f^8$ is observed, pointing out distinct thermally activated mechanisms for the population and deexcitation of the $^5D_4$ and $^5D_0$ levels, as detailed below.

The room-temperature excitation spectra for the $^5D_4$ ($Tb^{3+}$) and $^5D_0$ ($Eu^{3+}$) levels were monitored at the $^5D_4 \rightarrow {}^7F_6$ ($Tb^{3+}$) and $^5D_0 \rightarrow {}^7F_4$ ($Eu^{3+}$) transitions (Figures S5-S7 in Supporting Information). The $^5D_0 \rightarrow {}^7F_4$ transition was chosen to avoid overlap with the $^5D_4 \rightarrow {}^7F_3$ ($Tb^{3+}$) transition, thus, enabling the determination of the selective $Eu^{3+}$ excitation path. All the excitation spectra are dominated by a broadband in the UV with two main components at around 280 and 330 nm ascribed to the ligand's singlet excited states,[65] and of a series of narrow lines ascribed to the intra-$4f^8$ and intra-$4^6$ transitions in the excitation monitored at the $^5D_4 \rightarrow {}^7F_6$ ($Tb^{3+}$) and $^5D_0 \rightarrow {}^7F_4$ ($Eu^{3+}$) transitions, respectively. The negligible intensity of the intra-4f lines points out that the $Ln^{3+}$ excited states are mainly populated through ligands sensitization. Noticeably, it is detected the presence of $Tb^{3+}$ transitions ($^7F_6 \rightarrow {}^5D_{4-2}$, $^5G_{6,5}$, $^5L_{10,9}$) in the excitation spectra selectively monitored within the $^5D_0 \rightarrow {}^7F_4$ transition, pointing out $Tb^{3+}$-to-$Eu^{3+}$ energy transfer. Nonetheless, as the temperature is lowered, the relative intensity of such intra-4f$^8$ transition decreases being negligible around 175 K (inset of Figure S6 in Supporting Information). Therefore, the Tb$^{3+}$-to-Eu$^{3+}$ energy transfer is thermally activated ($T$>175 K) in accordance with our Ln$^{3+}$-to-Ln$^{3+}$ energy transfer calculations (see Supporting Information), where the Tb$^{3+}$-to-Eu$^{3+}$ energy transfer rate starts to overcome the Eu$^{3+}$-to-Tb$^{3+}$ in this range of temperature (Figure S19 in Supporting Information). This is related mainly to the increasing of the $^7F_1$ population (as depicted in Figure S17 in Supporting Information) once the main energy transfer pathway involves the $^7F_1 \rightarrow ^5D_1$ (Tb$^{3+}$-to-Eu$^{3+}$ energy transfer, pathway 11 in Table S9 in Supporting Information), while the other process (Eu$^{3+}$-to-Tb$^{3+}$) is independent of the $^7F_1$ population (Table S10 in Supporting Information). These energy transfer mechanisms will be discussed in detail in the following section 2.3, based on the thermal dependence of the energy transfer rates.

The contribution of the distinct excitation paths can be quantified through the absolute emission quantum yield ($Q$, Table S3), whose maximum value is attained under ligands excitation at 330 nm ($Q^{L}$=0.66±0.07). Lower values are found when the intra-4f levels are directly excited, pointing out the role of the ligands in the energy transfer processes. Interestingly, when the Eu$^{3+}$ is preferentially excited under direct intra-4f$^6$ excitation ($^5D_2$, 466 nm), a lower value ($Q^{Eu}$=0.08±0.01) is found when compared with that ($Q^{Tb}$=0.28±0.03) attained under intra-4f$^8$ excitation ($^5D_4$, 489 nm). When excited at 396 nm under a superposition of ligand and $^5L_6$ excitation a similar value is also found ($Q^{L,Eu}$=0.29±0.03).

The thermal dependence of the $^5D_4$ and $^5D_0$ lifetimes was studied by monitoring the emission decay curves of the $^5D_4 \rightarrow ^7F_5$ (Tb$^{3+}$, Figure S8 in Supporting Information) and $^5D_0 \rightarrow ^7F_2$ (Eu$^{3+}$, Figure S9 in Supporting Information) transitions. We note that the excitation spectra monitored in the $^5D_0 \rightarrow ^7F_2$ transition overlap those monitored in the $^5D_0 \rightarrow ^7F_4$ (Figure S7 in Supporting Information). We, therefore, chose the higher intensity transition to monitor the emission decay without losing selectivity. The emission decay curves are well described by a single exponential function revealing that whereas the $^5D_0$ lifetime ($\tau_{^5D_0}$) is nearly independent of the temperature, being $\tau_{^5D_0}$ =1.12±0.05

ms in the (12-450 K) range, the $^5$D$_4$ ($\tau_{^5D_4}$) lifetime decreases from $\tau_{^5D_4}$= 1.085±0.005 ms at 12 K to 0.019±0.005 ms at 450 K (Figure 3). Focusing on the $^5$D$_0$ emission decay curves measured within 225–325 K, there is evidence of a rise time (dependent on the temperature, Figure 3a and Figure S9 in Supporting Information) well described by:[66]

$$N(t) = \left[N_0 + N_1\left(1 - e^{\left(-\frac{t}{\tau_{rs}}\right)}\right)\right] e^{\left(-\frac{(t-t_0)}{\tau_{^5D_0}}\right)}, \qquad (1)$$

where $N_0$ is the $^5$D$_0$ population at $t$=0 and $N_1$ is the population at the same instant ($t$=0) in an upper feeding level; and $\tau_{rs}$ is the $^5$D$_0$ rise time. The best fit to the data points out that the calculated $\tau_{rs}$ values are similar to the $^5$D$_4$ lifetime determined independently from selective decay measurements (Figure 3b). This is evidence that $^5$D$_4$ is the upper feeding level supporting the presence of Tb$^{3+}$-to-Eu$^{3+}$ energy transfer above 175 K, as also confirmed by our theoretical Ln$^{3+}$-to-Ln$^{3+}$ energy transfer calculations (Figure S19 in Supporting Information). Intriguingly, the temperature, where the Tb$^{3+}$-to-Eu$^{3+}$ transfer becomes higher than the Eu$^{3+}$-to-Tb$^{3+}$ one, matches with the observation of the $^5$D$_0$ rise time. Even though the energy transfer from the ligands is faster than the Ln$^{3+}$-to-Ln$^{3+}$ one, when the excitation source is turned off, the Eu$^{3+}$ $^5$D$_0$ population rises owing to a delayed energy Tb$^{3+}$-to-Eu$^{3+}$ process. Besides, we emphasize the independence of the $^5$D$_0$ emission lifetime on the temperature.

The Ln$^{3+}$-to-Ln$^{3+}$ rates are in agreement with the experimental rates (in the order of hundreds s$^{-1}$) obtained by Liu *et al.* for [Ln(TFA)$_3$(TPPO)$_2$] (TFA=trifluoroacetylacetone, TPPO=triphenylphophine oxide, Ln= Tb$^{3+}$ and Eu$^{3+}$).[67] However, due to a large Tb$^{3+}$–Eu$^{3+}$ distance (7.7 Å), the calculated Ln$^{3+}$-to-Ln$^{3+}$ energy transfer rates (Tables S9 and S10 in Supporting Information) are orders of magnitude lower than the Ligand-to-Ln$^{3+}$ one (with $R_L$=4.12 Å) and, thus, can be omitted in the Eu$^{3+}$ $^5$D$_0$ and Tb$^{3+}$ $^5$D$_4$ populational analysis.

The fascinating thermal dependence of the optical features of **1**, shown in Figure 2, envisages its use as a novel luminescence thermometer and the relative intensities of the $^5D_4 \rightarrow ^7F_5$ ($I_{Tb}$) and $^5D_0 \rightarrow ^7F_2$ ($I_{Eu}$) transitions were quantified by integration of the emission spectra between 530-565 and 605-635 nm, respectively. We note that the spectral overlap (marked with an asterisk in Figure 2a) between the $^5D_0 \rightarrow ^7F_2$ ($Eu^{3+}$) and $^5D_4 \rightarrow ^7F_3$ ($Tb^{3+}$) transitions should be considered to avoid an overestimation of $I_{Eu}$ (Figure S10, S11 and further details in Supporting Information). Figure 2b shows that the $I_{Tb}$ remains approximately constant as the temperature is raised from 12 to 200 K, and decreases at $T$>200 K. A distinct behavior is noticed for the $I_{Eu}$ that increases from 12 to 350 K, remaining approximately constant for $T$>350 K (Figure 2c). These temperature dependencies in a ratiometric thermometer will be theoretically modeled in the next section.

## 2.3. 2.3 Modeling the thermal response

### 2.3.1. In silico experiments

**The time-dependent density functional theory (TD-DFT) calculation, using the optimized structure (Figures S14 and S15 in Supporting Information), was performed to obtain the centroid of the triplet $T_1$ and singlet $S_1$ states. Their energies ($T_1 \approx 21400$ cm$^{-1}$ and $S_1 \approx 29900$ cm$^{-1}$) were experimentally measured for the [Gd(bpy)$_2$(NO$_3$)$_3$] analog complex.[68, 69] The TD-DFT procedure allowed to estimate the donors–acceptors distances ($R_L$, Figure S14 in Supporting Information), quantities that are essential for the energy transfer calculations, and this can be obtained from the analysis of the molecular orbitals (MOs) compositions involved in the formation of $T_1$ and $S_1$, as depicted in Figure S15 in Supporting Information. It can be noted that the ligands $NO_3^-$ are not involved in the $T_1$ state. However, the $S_1$ state is characterized by an electronic density displacement from the occupied MOs at the $NO_3^-$ ligands to the unoccupied at the ancillary ligands bpy. Once both excited states $S_1$ and $T_1$ are localized through the bpy ligands (unoccupied MOs in Figure S15 in Supporting Information), implying that they have the same value of the donor-acceptor distance $R_L$=4.12 Å (Figure S14 in Supporting Information).**

### 2.3.2. Intramolecular energy transfer rates

**Based on the schematic energy level diagram for both, $Eu^{3+}$ and $Tb^{3+}$ complexes (Figure 4), we aim at visualizing how the intramolecular energy transfer (IET) rates play a fundamental role in the emission process. Since the bpy ligands are responsible for good absorption (pumping rate $\phi$, Eq. S22 in Supporting Information) of the incident light, efficient forward IET rates from $S_1$ ($W_S$) and $T_1$ ($W_T$) are desirable to populate the $Ln^{3+}$ emitting levels ($^5D_0$ and $^5D_4$), otherwise, no intra-f emission may be observed. Other fundamental quantities displayed in Figure 4 are the backward IET rates ($W_S^b$ and $W_T^b$), intersystem crossing $S_1$→$T_1$ rate ($W_{ISC}$), multiphonon relaxation from upper $Ln^{3+}$ levels to the emitting one ($W_{3\rightarrow 4}$), and decay lifetimes ($\tau_S$, $\tau_T$, $\tau$).**

**All IET pathways calculated (Tables S7 and S8 in Supporting Information) takes into account the selection rules on the *J* quantum number ($|J-J'| \leq \lambda \leq J+J'$ for the dipole-dipole and the dipole-multipole mechanisms, $\Delta J=0, \pm 1$ for the exchange mechanism)[70] and represent the rates obtained at 300 K. Considering the non-zero contributions, 60 forward IET pathways (30 for Ligand-to-$Eu^{3+}$ and 30 for Ligand-to-$Tb^{3+}$) were examined. Using the same procedure to calculate all 120 pathways (60 forward and 60 backward IET rates) but varying the temperature, we obtain the summarized data in Table 1.**

**It can be observed that, for the case of the $Tb^{3+}$ complex, only the backward energy transfer from $S_1$ ($W_S^b$) changes moderately with the temperature (Table 1). This is related to the ($^7F_6\rightarrow{}^5L_6$) →$S_1$ (pathway 7, Table S8) which has an energy difference between the donor and acceptor states ($\delta$) of the order of $k_BT$. This specific pathway is not important for the forward because the $S_1\rightarrow(^7F_6\rightarrow{}^5G_6)$ (pathway 3) is three orders of magnitude higher. From the $T_1$ channel ($W_T$ and $W_T^b$), there is a lack of predominant pathways with δ of the order of $k_BT$ (see Table S8). Therefore, the thermal behavior of the $Tb^{3+}$ complex is governed exclusively by its $^5D_4$ decay time ($\tau_{^5D_4}$, Figure 3b). Contrarily, the $Eu^{3+}$ complex has almost constant decay time ($\tau_{^5D_0}$, Figure 3b), showing however significant variations in the IET rates with the temperature increase. This is rationalized taking into account that the population of $^7F_1$ is increasing with the temperature[51] (Figure S17 in Supporting Information) once the main contributions are associated with pathways in which the $^7F_1$ is involved (see pathways 12, 21, and 23 in Table S7 in Supporting Information). Besides, pathway 23 ($T_1\rightarrow(^7F_1\rightarrow{}^5D_2)$, Table S7 in Supporting Information) has a strong temperature dependence owed to its δ in the order**

of $k_BT$. Moreover, an unusual behavior like an "energy transfer channel tuning", is also observed for the $Eu^{3+}$ which means that the population of the $^5D_0$ for low temperatures ($T$ < 125 K) is influenced by the $T_1 \rightarrow Eu^{3+}$ channel ($W_T$) while for $T \geq 125$ K, the $^5D_0$ level is more sensitive by the $S_1 \rightarrow Eu^{3+}$ channel ($W_S$), this is the reason we called energy transfer channel tuning. To support this effect, Figure S18 in Supporting Information reveals that the $W_T$ and $W_S$ have opposite trends when temperature increases. In summary, the uneven thermal dependence on the $I_{Eu}$ behavior can be explained by the relative magnitude of $W_{ISC}$ and $W_S$: *i*) for $T$ < 125 K, $W_{ISC} > W_S$, preferentially the triplet state is populated and thus energy flows from the lowest energy triplet state to the $Ln^{3+}$ ion ($T_1 \rightarrow Eu^{3+}$), whereas *ii*) for $T \geq 125$ K, $W_{ISC} < W_S$, and thus the singlet state tends to transfer energy directly to the $Eu^{3+}$ ion (the $S_1 \rightarrow Eu^{3+}$ energy transfer becomes dominant).

### 2.3.3. Rationalizing thermal dependence of the integrated intensities kinetics simulations

The kinetics of this system includes an equilibrium between rates of absorption, IET (both forward $W$ and backward $W^b$) rates, radiative and non-radiative decay rates. This kinetics can be defined by an appropriate set of ordinary differential equations (ODEs) which comprises the temporal behavior of the populations at each level. However, sometimes it is hard to describe and include the population of all levels of the $Ln^{3+}$ ion. To simplify the setup of the rate equations, groups of levels are represented by $|n\rangle$ (with the same indication as in Figure 4) and their respective population as $P_n$. Thus, based on the IET rates and the schematic energy level diagram (Figure 4), a 5-level set of ODEs with initial conditions (when $t$=0 s) is given by:

| ODE | Initial condition | Level (or Levels) | |
|---|---|---|---|
| $\frac{d}{dt}P_0(t) = -\phi P_0(t) + \frac{1}{\tau_T}P_1(t) + \frac{1}{\tau_S}P_2(t) + \frac{1}{\tau}P_4(t)$ | $P_0(0) = 1$ | $S_0$ and $^7F_J$ | (2) |
| $\frac{d}{dt}P_1(t) = -\left(\frac{1}{\tau_T} + W_T\right)P_1(t) + W_{ISC}P_2(t) + W_T^bP_3(t)$ | $P_1(0) = 0$ | $T_1$ | (3) |
| $\frac{d}{dt}P_2(t) = -\left(\frac{1}{\tau_S} + W_{ISC} + W_S\right)P_2(t) + \phi P_0(t) + W_S^bP_3(t)$ | $P_2(0) = 0$ | $S_1$ | (4) |

$$\frac{d}{dt}P_3(t) = -\left(W_{3\to4} + W_T^b + W_S^b\right)P_3(t) + W_S P_2(t) \qquad P_3(0) = 0 \qquad \begin{matrix} ^5\mathrm{D}_2 \text{ to } {}^5\mathrm{L}_{10}\ (\mathrm{Eu}^{3+}) \\ ^5\mathrm{D}_3 \text{ to } {}^5\mathrm{F}_5\ (\mathrm{Tb}^{3+}) \end{matrix} \tag{5}$$

$$\frac{d}{dt}P_4(t) = -\left(\frac{1}{\tau}\right)P_4(t) + W_{3\to4}P_3(t) + W_T P_1(t) \qquad P_4(0) = 0 \qquad \begin{matrix} ^5\mathrm{D}_{0,1}\ (\mathrm{Eu}^{3+}) \\ ^5\mathrm{D}_4\ (\mathrm{Tb}^{3+}) \end{matrix} \tag{6}$$

**The lifetime values of the ligands used to solve the equations above, $\tau_T = 10^{-3}$ s and $\tau_S = 10^{-9}$ s, are typical values found in the literature.[71, 72] If we change them to one order of magnitude, for example, the population of the emitting level will decrease ($\tau_S$~$10^{-10}$ s) or increase ($\tau_S$ ~ $10^{-8}$) almost one order of magnitude too. The $Ln^{3+}$ emitting level is less sensitive to the $\tau_T$, varying less than 1% when we increase/decrease the lifetime. We need to keep in mind that the decay rate of the $T_1$ is ~$10^3$ $s^{-1}$ ($1/\tau_T$) and the $T_1 \to Ln^{3+}$ is ~$10^6$ $s^{-1}$ (for the $Eu^{3+}$ complex), explaining this weak variation. On contrary, the decay rate of $S_1$ is $10^9$ $s^{-1}$ ($1/\tau_S$), while the $S_1 \to Ln^{3+}$ is in the order of $10^5$ $s^{-1}$ (also for the $Eu^{3+}$ complex), thus these competitions influence the $Ln^{3+}$ emitting level population. However, once we are dealing with the ratio between intensities in two analogs complexes (they must present almost equal values of $\tau_S$ and $\tau_T$), this difference cancels in the thermometric parameter and consequently in the thermal sensitivity. Except for the intersystem crossing rate which is almost constant with temperature,[73] the $\tau_S$, $\tau_T$, and $W_{3\to4}$ might be dependent on the temperature as well. Therefore, as a proof of concept, we made simulations on the ratio between the populations of emitting levels ($Tb^{3+}$ $^5D_4$ and $Eu^{3+}$ $^5D_0$) varying these rates two orders of magnitude each and we found that the thermal behavior remains unchanged (see Figures S21 and S22 and discussions around). For the $Ln^{3+}$ lifetimes $\tau$, the experimental values were used (Figure 3b). As mentioned before, $W_{ISC}$ is the intersystem crossing rate ($S_1 \to T_1$), which is very sensitive to the energy gap between these states[74, 75] and such energy gap of *ca.* 8500 $cm^{-1}$ may lead to a reasonable value of $W_{ISC}$~$10^5$ $s^{-1}$. $W_{3\to4}$ is the nonradiative energy decay from upper levels of $Ln^{3+}$ to the emitting levels ($^5D_0$ and $^5D_4$), which is in the order of ~$10^6$ $s^{-1}$ for $Ln^{3+}$-chelates.[70] The set of ODEs (Eqs. 2–6) were numerically solved using the Radau method.[76] As an illustration, Figure S20 in Supporting Information shows the transient behavior of the population fractions of the $^5D_0$ and $^5D_4$ with the temperature. Notably, the $^5D_0$ presents a population increasing while the $^5D_4$ presents the opposite trend.**

**These observations corroborate the experimental intensities depicted in Figure 2b,c, as the populations of the emitting states are in the steady-state regime (when $\frac{d}{dt}P_4(t) = 0$, Table S11 in Supporting Information).**

### 2.3.4. Theoretical and experimental thermometry

Once the $Eu^{3+}$ $^5D_0$ and $Tb^{3+}$ $^5D_4$ emitting levels populations are estimated, we will demonstrate how the behavior of experimental thermometric parameter Δ and the relative thermal sensitivity (Eq. S1 in Supporting Information), can be explained and predicted from the basics of the theory of luminescent energy transfer, through the Judd-Ofelt theory,[77, 78] IET theory,[79] and the populational analysis from rate equations.[80] Thus, we can describe the $Tb^{3+}$ $^5D_4 \rightarrow {}^7F_5$ and $Eu^{3+}$ $^5D_0 \rightarrow {}^7F_2$ intensities ($I_{Tb}$ and $I_{Eu}$, respectively) and consequently the thermometric parameter $\Delta = I_{Tb}/I_{Eu}$.

The relative amount of $Tb^{3+}$ and $Eu^{3+}$ does not substantially impact the kinetics and the emitting level populations. Since each $Ln^{3+}$ is located in a single molecular entity $[Ln(bpy)_2(NO_3)_3]$, the minimal distance between two $Ln^{3+}$ centers will be kept at 7.7 Å. For example, if we consider the composition of 50% $Tb^{3+}$ and 50% $Eu^{3+}$, the system $[Tb_{0.5}Eu_{0.5}(bpy)_2(NO_3)_3]$ will present a minimal intermolecular $Tb^{3+}$-$Eu^{3+}$ distance of 7.7 Å and the $Ln^{3+}$-to-$Ln^{3+}$ rates will undergo a little dependency on the distribution of the ions in the matrix but still produces low $Ln^{3+}$-to-$Ln^{3+}$ energy transfer rates (in the order of $10^2$ $s^{-1}$). Besides, as discussed before, the kinetics is dominated by the intramolecular energy transfer (Ligand-to-$Ln^{3+}$) part which is orders of magnitude higher than the intermolecular energy transfer ($Ln^{3+}$-to-$Ln^{3+}$), thus the $Tb^{3+}/Eu^{3+}$ ratio will not significantly change the kinetics and the emitting level populations. The inclusion of such low rates of $10^2$ $s^{-1}$ ($Ln^{3+}$-to-$Ln^{3+}$ energy transfer) will not contribute to a significant change of the two emitting levels ($^5D_4$ and $^5D_0$) populations. Just for illustrating, if we consider the $Tb^{3+}$-to-$Eu^{3+}$ rates in a 7-levels set of ODEs, this rate will compete with the backward IET $Tb^{3+} \rightarrow T_1$ rate which is temperature independent ($W_T^b = 4.18\times10^6$ $s^{-1}$, Table 1) and it populates the $T_1$ instead of the $^5D_0$ level. We should emphasize that this characteristic is exclusive due to the large $Tb^{3+}$-$Eu^{3+}$ distance involved.

Figure 5 presents the calculated and measured data of Δ together with the corresponding relative thermal sensitivities. It is evident the very nice agreement between calculated and measured data. The maximum $S_r$ value, 2.0 %·K$^{-1}$ at 262 K (and 1.6 %·K$^{-1}$ at 300 K), is comparable to the values reported in the literature for mixtures of Eu$^{3+}$ and Tb$^{3+}$ complexes[1] and MOFs operating near room temperature[41, 51] (Table S4 in Supporting Information). Remarkably, the high thermal stability of **1** could be taken as an advantage to investigate the repeatability of the temperature sensing in the room temperature region (where the $S_r$ is relatively large) upon thermal cycling. It turns out that **1** exhibits an exceptional 97% repeatability of *Δ* over 10 temperature cycles between 300 and 325 K (Fig. S13, SI). Yet, the thermal stability of **1** up to 560 K and the absence of solvate in the crystal lattice suggest it might also be utilized in a higher temperature range. Moreover, we should emphasize that this is the first time where the thermometric parameters and sensitivity are modeled from theory and it should be a step toward predictions of thermometric properties before the nanothermometers preparation (Figures S12-S13 in the Supporting Information).

**In the literature, the sigmoidal-shaped temperature dependence of the integrated intensities is frequently fitted to a semi-classical Mott-Seitz model.[35, 51] When a ratio of integrated intensities is considered, it is common to assume that it is dominated by the temperature dependence of one transition presenting the sigmoidal functional form,[51] assuming, thus, that the other transition is virtually temperature independent. It is easy to understand that this is a demanding assumption that generally is not observed in practice. On the contrary, the theoretical approach presented here can model both the thermal quenching of the $^5D_4 \rightarrow {}^7F_5$ transition and the thermal raise of the $^5D_0 \rightarrow {}^7F_2$ one (that is the thermometric parameter Δ) permitting, thus, to understand how $S_r$ can be optimized. Attending to its definition (Eq. S1 in Supporting Information), to increase $S_r$ we must diminish Δ and this can be achieved by decreasing the integrated intensity of the Tb$^{3+}$ $^5D_4 \rightarrow {}^7F_5$ transition and/or increasing that of the Eu$^{3+}$ $^5D_0 \rightarrow {}^7F_2$ line. The former is ruled out by the $^5D_4$ state lifetime, whereas the latter is controlled by the energy gap between the $^7F_0$ and $^7F_1$ states and the energy of the singlet and triplet states of the ligand, which must favor the forward IET rate. The energy gap between the $^7F_0$ and $^7F_1$ states (Fig. S17 in Supporting Information) might be experimentally controlled by a**

**change of the ligands as well as by the fine-tuning in the coordination sphere of the lanthanide to reshape the crystal field splitting. The ability to model the temperature dependence of the two integrated intensities opens the possibility to predict $S_r(T)$ giving precious hints on the energy transfer processes that regulate the operating temperature range of dual-center Eu/Tb molecular thermometers.**

**The guidelines to performing theoretical predictions on thermometric properties could be summarized into four steps: *i)* structure of the compound, *ii)* energies of the singlet and triplet states and their distances to the $Ln^{3+}$ center (donor-acceptor distances), *iii)* IET rates (backward and forward), *iv)* rate equations model to determining the population of the emitting levels. We must emphasize that in the present case the $Tb^{3+}$-to-$Eu^{3+}$ energy transfer is not operative due to a large $Tb^{3+}$-$Eu^{3+}$ distance (~7.7 Å). In the opposite case, these rates should be included in step *iv)* above.**

## 3. 4. Conclusions

**This work provides a comprehensive analysis and rationalization of the mechanisms underpinning the temperature dependence of molecular thermometers. As an illustrative example, we rationalize the thermometric characteristics in a robust and thermally stable coordination complex, $[Tb_{0.94}Eu_{0.06}(bpy)_2(NO_3)_3]$, exhibiting a high thermal sensing reproducibility (> 97%) for a molecule-based material. The investigated complex is easily synthesized in large yields, presenting an efficient $Ln^{3+}$ sensitization by the bpy ligands together with chemical stability in air and water, and the absence of solvent molecules in the first coordination shell.**

In this work, we modeled a dual-center $Ln^{3+}$-based luminescent thermometer through the Judd-Ofelt theory, intramolecular energy transfer theory, and the populational analysis from rate equations, furnishing a clear picture of the temperature dependence of the luminescence spectrum. To our knowledge, this constitutes the first example in which the functional form of the thermal dependence of the integrated areas could be accurately anticipated, enabling thus the prediction of the thermometric parameter $\Delta$ and of the relative thermal sensitivity. Moreover, this approach is a toolbox that can be taken as an advantage to guide the design of novel molecular thermometers based on dual-emissive centers. The required inputs are basic structural parameters (*e.g.* the $Ln^{3+}$-$Ln^{3+}$ distance) and the energies of singlet and triplet states of the ligands used. The implementation of these computational procedures such as machine learning and/or data mining could be useful to indicate which systems (or a class of) will give the best responses for operating in the desired range of temperature (*e.g.* biological and cryogenic).

In clear contrast with the usual trial and error fitting methods, this rational modeling will open an avenue for intelligently engineering optimized dual-center thermometers that could be subsequently integrated into future devices.

## 4. 5. Experimental Section

***Reagents and Chemicals*****: All chemical reagents were purchased and used without further purification: Terbium nitrate hexahydrate (ABCR, 99.9% (REO)), Europium nitrate hexahydrate (Alfa Aesar, 99.9% (REO)), 2,2'-bypyridine (Sigma Aldrich, >99%), ethanol absolute (100% PA, VWR). All experiments were carried out under aerobic conditions.**

***Synthesis of [$Tb_{0.94}Eu_{0.06}(bpy)_2(NO_3)_3$] (1)*****: A 30 mL hot ethanolic solution of 2,2'-bipyridine (0.800 mmol, 125 mg) was added dropwise to 30 mL of a hot ethanolic solution containing a 95/5 mixture $Tb(NO_3)_3{\cdot}6H_2O$ (0.380 mmol, 172 mg) and $Eu(NO_3)_3{\cdot}6H_2O$ (0.020 mmol, 9 mg). A white precipitate formed immediately. 50 mL of ethanol was subsequently added to obtain a clear solution before being filtered. Slow evaporation of the resulting solution gives single-crystals of 1. Yield = 39 %. EDS: 5.54/94.46 (Eu/Tb). The compound could also be obtained in a better yield and larger amount by the simple precipitation of the molecular precursors. For instance, a 30 mL hot ethanolic solution of 2,2'-bipyridine (2.200 mmol, 343 mg) was added dropwise to a hot ethanolic solution of 95/5 mixture $Tb(NO_3)_3{\cdot}6H_2O$ (1.045 mmol, 474 mg) and $Eu(NO_3)_3{\cdot}6H_2O$ (0.055 mmol, 24 mg). A white precipitate formed immediately, and the reaction mixture was kept at 70°C for about 10 min. Then the resulting precipitate was recovered by filtration, washed several times, and dried in the air at room temperature. Yield = 82 %. EDS: 5.95/94.05 (Eu/Tb). Elemental analysis calcd. for $Tb_{0.94}Eu_{0.06}C_{20}H_{16}N_7O_9$ (%): C, 36.57; H, 2.46; N, 14.93; found (%): C, 36.13; H, 2.51; N, 14.68. IR (KBr): $\nu$(O-H) = 3429 $cm^{-1}$ (residual ethanol), $\nu$(C-H)=3100-2500 $cm^{-1}$ (C-H aromatic), $\nu$(C=C and C=N)=1605-1438 $cm^{-1}$ (aromatic ring), $\nu$($NO_3^-$)=1384 $cm^{-1}$**

**(nitrate), $\nu$(C=C and C=N)=1328-1259 cm$^{-1}$ (aromatic ring stretch), $\nu$(C=C and C-H)=1244-894 (ring stretch + inter-ring stretch, ring-H stretch), $\nu$($NO_3^-$)=815-809 cm$^{-1}$ (nitrate), $\nu$(C=C and C-H)=771-627 (ring-H out-of-plan bend), $\delta$(C=C)=465 cm$^{-1}$ (inter-ring deformation), $\delta$(C=C)=434-414 cm$^{-1}$ (ring torsion).**

*Structural and Photophysical Characterization*: Elemental analysis was performed with an analyzer Elementar Vario MICRO Cube. Powders were pyrolyzed at 1150 °C and then reduced at 850 °C over hot Copper. Infrared spectra were recorded as KBr disks (1 wt% of sample) in the range 4000–400 cm$^{-1}$ on a PerkinElmer Spectrum two spectrophotometer with 8 acquisitions. A background without sample was recorded before the measurements.

X-ray powder diffraction patterns were recorded in the $2\theta$ interval 5-60° at room temperature with the PANalytical X'Pert Powder analytical diffractometer mounted in a Debye−Scherrer configuration and equipped with Cu radiation ($\lambda$=1.5418 Å).

Thermogravimetric analyses were obtained with a thermal analyser STA 409 Luxx® (Netzsch) in the range 25–650 °C at a heating speed of 5 °C.min$^{-1}$.

Scanning Electronic Microscopy (EDS) analyses were performed on FEI Quanta FEG 200 instrument. The powders were deposited on an adhesive carbon film and analyzed under vacuum. The quantification of the heavy elements was carried out with the INCA software, with a dwell time of 3 $\mu$s.

Magnetic susceptibility data were collected with a Quantum Design MPMS-XL SQUID magnetometer working in the range 1.8–350 K with a magnetic field up to 7 Tesla. The AC magnetic susceptibility measurements were carried out in the presence of a 3 Oe oscillating field in zero or applied external DC field.

The photoluminescence measurements were recorded using a Fluorolog3® Horiba Scientific (Model FL3-22) spectroscope, with a modular double grating excitation spectrometer (fitted with a 1200 grooves/mm grating blazed at 330 nm) and a TRIAX 320 single emission monochromator TRIAX 320 single emission monochromator (fitted with a 1200 grooves/mm grating blazed at 500 nm, reciprocal linear density of 2.6 nm.mm$^{-1}$). The excitation source was a 450 W Xe arc lamp. Emission spectra (acquired using the front face mode) were corrected for the spectral response of the monochromators and detector, using the correction spectrum provided by the manufacturer, and the excitation spectra were corrected for the spectral distribution of the lamp intensity recorded using a photodiode reference detector. The time-resolved emission spectra and emission decay curves were acquired with the same instrumentation using a pulsed Xe–Hg lamp (6 $\mu$s pulse at half-width and 20–30 $\mu$s tail). The temperature was varied using a helium-closed cycle cryostat, a vacuum system (4×10$^{-4}$ Pa), and an autotuning temperature controller (Lakeshore 330, Lakeshore) with a resistance heater. All the measurements began at least 300 s after the temperature indicated in the temperature controller remained constant, thus ensuring the samples thermalization and constant temperature during the measurement.

The emission quantum yield values were measured at room temperature using a system (C9920-02, Hamamatsu) with a 150 W xenon lamp coupled to a monochromator for wavelength discrimination, an integrating sphere as the sample chamber, and a multichannel analyzer for signal detection. Three measurements were made for each sample and the average values obtained are reported with accuracy within 10% according to the manufacturer.

***X-Ray crystallography:*** **The crystal of 1, with dimensions 0.049 mm x 0.093 mm x 0.113 mm, was measured by single crystal x-ray diffraction using an exposure time of 3.71 hours. Frames integration was performed using a narrow-frame algorithm with the Bruker SAINT software package. The integration of the data using an orthorhombic unit cell yielded a total of 73161 reflections to a maximum $\theta$ angle of 45.29° (0.50 Å resolution), of which 9480 were independent (average redundancy 7.717, completeness = 100.0%, $R_{int}$ = 4.09%, $R_{sig}$ = 2.82%) and 6366 (67.15%) were greater than 2σ(F2). The final obtained unit cell parameters: *a* = 9.0395(3) Å, *b* = 15.0022(5) Å, *c* = 16.7187(6) Å, volume = 2267.3(2) Å$^3$, are based upon the refinement of the XYZ-centroids of 5700**

**reflections above 20 σ(I) with 4.855° < 2θ < 84.71°. Data were corrected for absorption effects using the Multi-Scan method (SADABS). The ratio of minimum to maximum apparent transmission was 0.832. The structure solution was solved and refined using the Bruker SHELXTL Software Package, with $Z = 4$ for the formula unit, $Tb_{0.95}Eu_{0.05}C_{20}H_{16}N_7O_9$. The Ln (Eu, Tb) atomic positions, which are located on the 4c Wyckoff sites(1/2,y+1/2,1/4), were refined and the calculated occupations are in agreement with both those expected from the synthesis ($Eu_{0.05}Tb_{0.95}$) and those obtained from EDX characterization ($Eu_{0.06}Tb_{0.94}$).The final anisotropic full-matrix least-squares refinement on F2 with 175 variables converged at $R_1 = 2.92\%$, for the observed data and $w_{R2} = 6.57\%$ for all data. The goodness-of-fit was 1.110. The largest peak in the final difference electron density synthesis was 1.168 e-/Å$^3$ and the largest hole was -2.342 e-/Å$^3$ with an RMS deviation of 0.312 e-/Å$^3$. On the basis of the final model, the calculated density was 1.924 g/cm$^3$ and F(000), 1287 e-.**

**CCDC–2079476 (1) contains the supplementary crystallographic data for this paper. These data are provided free of charge by The Cambridge Crystallographic Data Centre: ccdc.cam.ac.uk/structures. The corresponding CIF files are also available in the Supporting Information.**

## 5. 6. Theoretical Section

***In silico experiments*: Density functional theory (DFT) calculations were used to obtain structural and electronic properties like molecular geometry, symmetry, and molecular orbitals (MOs) compositions of the states involved in the energy transfer process. The geometry optimization was performed using the Gaussian 09 program[81] with B3LYP functional.[82, 83] The geometry optimization was performed using the Gaussian 09 program[81] with B3LYP functional.[82, 83] A Pople's basis set 6-31G(d) was employed to nonmetal atoms (hydrogen, carbon, nitrogen, oxygen, fluorine, and silicon) and the $Ln^{3+}$ ion was treated with MWB52 or MWB54 ($Ln^{3+} = Eu^{3+}$ or $Tb^{3+}$, respectively) basis set.[84] The time-dependent density functional theory (TD-DFT) calculation, using the same functional and basis set, was used to obtain the geometric centroid of the excited singlet ($S_1$) and triplet ($T_1$) states. This procedure allows estimating the donors–acceptors distances $R_L$, quantities that are essential for the energy transfer calculations.**

***Energy transfer rates*: The intramolecular energy transfer rates (IET) from the excited states $S_1$ and $T_1$ to the $Ln^{3+}$ ion was calculated considering the dipole-dipole ($W_{d-d}$, Eq. S9), dipole-multipole ($W_{d-m}$, Eq. S10) and exchange ($W_{ex}$, Eq. S11) mechanisms. Thus,**

**the forward energy transfer rates ($W_S$ and $W_T$) are given by the sum of these three mechanisms (Eq. S13). The resonance (or energy mismatch) conditions $\delta = E_L - E_{Ln}$ (the donor-acceptor energy difference) was included by Malta[79] in an analytical expression (Eq. S12) for the spectral overlap integral, well-examined by Smentek and Kędziorski.[85] The shape of the spectral overlap as a function of the bandwidth at half-height of the ligand's state ($\gamma_L$) and the $\delta$ conditions can also be found in Moura Jr. *et al.*.[86] The backward energy transfer rates ($W^b$), the energy returned from acceptor ($Ln^{3+}$) to donor state ($S_1$ or $T_1$), are obtained by the Boltzmann's factor $\exp(-|\delta|/k_B T)$. See ESI for further detail. Particularly, the thermal behavior of the energy transfer rates can be calculated using Boltzmann's factor. However, in the case of $Eu^{3+}$, the thermally coupled populations of the levels $^7F_0$ and $^7F_1$ should be considered once their populations are the starting point when the energy transfer occurs.[51]**

***Level population analysis*: After all rates involved in the complexes are determined, the level population kinetics was described by a set of ordinary differential equations, [70, 80, 87]**

$$\frac{dP_i}{dt} = \sum_{j=1} W_{j\to i} P_j - \sum_{j=1} W_{i\to j} P_i \qquad (7)$$

where the summations run all levels of the system. $P_i$ and $P_j$ are the populations of the levels $|i\rangle$ and $|j\rangle$, the $W_{j\to i}$ and $W_{i\to j}$ are the energy transfer rates between these states. The appropriate set of rate equations, with their respective initial conditions, were numerically treated using the Radau method [76] in simulations from 0 to 10 ms with a step-size of 10 $\mu$s.

## *6.* Supporting Information

Supporting Information is available from the Wiley Online Library or from the author.

## 7. Acknowledgements

This work was developed within the scope of the projects CICECO-Aveiro Institute of Materials (UIDB/50011/2020 & UIDP/50011/2020) financed by Portuguese funds through the FCT/MEC and when appropriate co-financed by FEDER under the PT2020 Partnership Agreement. The support of the European Union's Horizon 2020 FET Open program under grant agreement No. 801305 (NanoTBTech) is also acknowledged. AMPB thanks the NanoHeatControl project (POCI-01-0145-FEDER-031469) for the post-doctoral grant. The authors also thank the University of Montpellier, CNRS and PAC of ICGM.

*Received:* ((will be filled in by the editorial staff))

*Revised:* ((will be filled in by the editorial staff))

*Published online:* ((will be filled in by the editorial staff))

## 8. References

[1] C. D. S. Brites, S. Balabhadra, L. D. Carlos, *Adv. Opt. Mater.* **2019**, *7*, 1801239.

[2] S. W. Allison, *Meas. Sci. Technol.* **2019**, *30*, 072001.

[3] C. D. S. Brites, P. P. Lima, N. J. O. Silva, A. Millán, V. S. Amaral, F. Palacio, L. D. Carlos, *Nanoscale* **2012**, *4*, 4799.

[4] D. Jaque, F. Vetrone, *Nanoscale* **2012**, *4*, 4301.

[5] M. Quintanilla, L. M. Liz-Marzan, *Nano Today* **2018**, *19*, 126.

[6] M. D. Dramicanin, *J. Appl. Phys.* **2020**, *128*, 040902.

[7] H. Suo, X. Q. Zhao, Z. Y. Zhang, Y. Wang, J. S. Sun, M. K. Jin, C. F. Guo, *Laser Photonics Rev.* **2021**, *15*, 2000319.

[8] E. Hemmer, P. Acosta-Mora, J. Mendez-Ramos, S. Fischer, *J. Mater. Chem. B* **2017**, *5*, 4365.

[9] J. J. Zhou, B. del Rosal, D. Jaque, S. Uchiyama, D. Y. Jin, *Nat. Methods* **2020**, *17*, 967.

[10] A. Bednarkiewicz, L. Marciniak, L. D. Carlos, D. Jaque, *Nanoscale* **2020**, *12*, 14405.

[11] M. Xu, X. M. Zou, Q. Q. Su, W. Yuan, C. Cao, Q. H. Wang, X. J. Zhu, W. Feng, F. Y. Li, *Nat. Commun.* **2018**, *9*, 2698.

[12] Y. L. Shen, H. D. A. Santos, E. C. Ximendes, J. Lifante, A. Sanz-Portilla, L. Monge, N. Fernandez, I. C. Coria, C. Jacinto, C. D. S. Brites, L. D. Carlos, A. Benayas, M. C. Iglesias-de la Cruz, D. Jaque, *Adv. Funct. Mater.* **2020**, *30*, 2002730.

[13] N. Inada, N. Fukuda, T. Hayashi, S. Uchiyama, *Nat. Protoc.* **2019**, *14*, 1293.

[14] R. Pinol, J. Zeler, C. D. S. Brites, Y. Y. Gu, P. Tellez, A. N. C. Neto, T. E. da Silva, R. Moreno-Loshuertos, P. Fernandez-Silva, A. I. Gallego, L. Martinez-Lostao, A. Martinez, L. D. Carlos, A. Millan, *Nano Lett.* **2020**, *20*, 6466.

[15] R. G. Geitenbeek, A. E. Nieuwelink, T. S. Jacobs, B. B. V. Salzmann, J. Goetze, A. Meijerink, B. M. Weckhuysen, *ACS Catal.* **2018**, *8*, 2397.

[16] T. Hartman, R. G. Geitenbeek, G. T. Whiting, B. M. Weckhuysen, *Nat. Catal.* **2019**, *2*, 986.

[17] C. D. S. Brites, P. P. Lima, N. J. O. Silva, A. Millán, V. S. Amaral, F. Palacio, L. D. Carlos, *Front. Chem.* **2013**, *1*, 9.

[18] J. Drabik, L. Marciniak, *ACS Appl. Mater. Inter.* **2021**, *13*, 1261.

[19] O. A. Savchuk, J. J. Carvajal, C. Cascales, J. Massons, M. Aguilo, F. Diaz, *J. Mater. Chem. C* **2016**, *4*, 6602.

[20] J. F. C. B. Ramalho, S. F. H. Correia, L. S. Fu, L. L. F. Antonio, C. D. S. Brites, P. S. Andre, R. A. S. Ferreira, L. D. Carlos, *Adv. Sci.* **2019**, *6*, 1900950.

[21] G. Brunet, R. Marin, M.-J. Monk, U. Resch-Genger, D. A. Gálico, F. A. Sigoli, E. A. Suturina, E. Hemmer, M. Murugesu, *Chem. Sci.* **2019**, *10*, 6799.

[22] D. Errulat, R. Marin, D. A. Gálico, K. L. M. Harriman, A. Pialat, B. Gabidullin, F. Iikawa, O. D. D. Couto Jr., J. O. Moilanen, E. Hemmer, F. A. Sigoli, M. Murugesu, *ACS Cent. Sci.* **2019**, *5*, 1187.

[23] M. Fondo, J. Corredoira-Vazquez, A. M. Garcia-Deibe, J. Sanmartin-Matalobos, M. Amoza, A. M. P. Botas, R. A. S. Ferreira, L. D. Carlos, E. Colacio, *Inorg. Chem. Front.* **2020**, *7*, 3019.

[24] J. H. Wang, J. J. Zakrzewski, M. Zychowicz, V. Vieru, L. F. Chibotaru, K. Nakabayashi, S. Chorazy, S. Ohkoshi, *Chem. Sci.* **2021**, *12*, 730.

[25] M. Runowski, P. Wozny, S. Lis, V. Lavin, I. R. Martin, *Adv. Mater. Technol.* **2020**, *5*.

[26] R. G. Geitenbeek, J. C. Vollenbroek, H. M. H. Weijgertze, C. B. M. Tregouet, A. E. Nieuwelink, C. L. Kennedy, B. M. Weckhuysen, D. Lohse, A. van Blaaderen, A. van den Berg, M. Odijk, A. Meijerink, *Lab Chip* **2019**, *19*, 1236.

[27] L. Rosso, S. Tabandeh, G. Beltramino, V. Fernicola, *Meas. Sci. Technol.* **2020**, *31*, 034002.

[28] E. C. Ximendes, W. Q. Santos, U. Rocha, U. K. Kagola, F. Sanz-Rodriguez, N. Fernandez, A. D. Gouveia-Neto, D. Bravo, A. M. Domingo, B. del Rosal, C. D. S. Brites, L. D. Carlos, D. Jaque, C. Jacinto, *Nano Lett.* **2016**, *16*, 1695.

[29] C. D. Brites, X. Xie, M. L. Debasu, X. Qin, R. Chen, W. Huang, J. Rocha, X. Liu, L. D. Carlos, *Nat. Nanotechnol.* **2016**, *11*, 851.

[30] C. D. S. Brites, M. C. Fuertes, P. C. Angelomé, E. D. Martínez, P. P. Lima, G. J. A. A. Soler-Illia, L. D. Carlos, *Nano Lett.* **2017**, *17*, 4746.

[31] O. A. Savchuk, J. J. Carvajal, C. D. S. Brites, L. D. Carlos, M. Aguilo, F. Diaz, *Nanoscale* **2018**, *10*, 6602.

[32] A. R. N. Bastos, C. D. S. Brites, P. A. Rojas-Gutierrez, C. DeWolf, R. A. S. Ferreira, J. A. Capobianco, L. D. Carlos, *Adv. Funct. Mater.* **2019**, *29*, 1905474.

[33] M. Back, J. Ueda, J. Xu, D. Murata, M. G. Brik, S. Tanabe, *ACS Appl. Mater. Inter.* **2019**, *11*, 38937.

[34] E. J. McLaurin, L. R. Bradshaw, D. R. Gamelin, *Chem. Mater.* **2013**, *25*, 1283.

[35] C. D. S. Brites, A. Millán, L. D. Carlos, in *Handbook on the Physics and Chemistry of Rare Earths*, Vol. 49 (Eds: J.-C. G. Bünzli, V. K. Pecharsky), Elsevier Science, B. V., Amsterdam 2016, 339.

[36] Y. Cheng, Y. Gao, H. Lin, F. Huang, Y. Wang, *J. Mater. Chem. C* **2018**, *6*, 7462.

[37] M. C. Jia, Z. Sun, M. X. Zhang, H. Y. Xu, Z. L. Fu, *Nanoscale* **2020**, *12*, 20776.

[38] R. G. Geitenbeek, H. W. de Wijn, A. Meijerink, *Phys. Rev. Appl.* **2018**, *10*, 064006.

[39] M. Suta, A. Meijerink, *Adv. Theor. Simul.* **2020**, *3*, 2000176.

[40] Y. Zhou, B. Yan, *Nanoscale* **2015**, *7*, 4063.

[41] J. Rocha, C. D. S. Brites, L. D. Carlos, *Chem. Eur. J.* **2016**, *22*, 14782.

[42] A. M. Kaczmarek, Y. Y. Liu, M. K. Kaczmarek, H. S. Liu, F. Artizzu, L. D. Carlos, P. Van Der Voort, *Angew. Chem. Int. Edit.* **2020**, *59*, 1932.

[43] L. Marciniak, A. Pilch, S. Arabasz, D. Jin, A. Bednarkiewicz, *Nanoscale* **2017**, *9*, 8288.

[44] C. Hazra, A. Skripka, S. J. L. Ribeiro, F. Vetrone, *Adv. Opt. Mater.* **2020**, *8*, 2001178.

[45] M. Back, J. Ueda, H. Nambu, M. Fujita, A. Yamamoto, H. Yoshida, H. Tanaka, M. G. Brik, S. Tanabe, *Adv. Opt. Mat.* **2021**, 10.1002/adom.202100033.

[46] L. Marciniak, A. Bednarkiewicz, J. Drabik, K. Trejgis, W. Strek, *Phys. Chem. Chem. Phys.* **2017**, *19*, 7343.

[47] C. D. S. Brites, K. Fiaczyk, J. F. C. B. Ramalho, M. Sojka, L. D. Carlos, E. Zych, *Adv. Opt. Mater.* **2018**, *6*, 1701318.

[48] C. D. S. Brites, P. P. Lima, N. J. O. Silva, A. Millán, V. S. Amaral, F. Palacio, L. D. Carlos, *Adv. Mater.* **2010**, *22*, 4499.

[49] A. Cadiau, C. D. S. Brites, P. M. F. J. Costa, R. A. S. Ferreira, J. Rocha, L. D. Carlos, *ACS Nano* **2013**, *7*, 7213.

[50] R. Piñol, C. D. S. Brites, R. Bustamante, A. Martínez, N. J. O. Silva, J. L. Murillo, R. Cases, J. Carrey, C. Estepa, C. Sosa, F. Palacio, L. D. Carlos, A. Millán, *ACS Nano* **2015**, *9*, 3134.

[51] V. Trannoy, A. N. Carneiro Neto, C. D. S. Brites, L. D. Carlos, H. Serier-Brault, *Adv. Opt. Mat.* **2021**, *9*, 2001938.

[52] T. P. van Swieten, D. C. Yu, T. Yu, S. J. W. Vonk, M. Suta, Q. Y. Zhang, A. Meijerink, F. T. Rabouw, *Adv. Opt. Mater.* **2021**, *9*, 2001518.

[53] S. Balabhadra, M. L. Debasu, C. D. S. Brites, R. A. S. Ferreira, L. D. Carlos, *J. Phys. Chem. C* **2017**, *121*, 13962.

[54] L. Ouahab, *Multifunctional molecular materials*, Pan Stanford, Singapore 2013.

[55] J.-C. G. Bünzli, C. Piguet, *Chem. Soc. Rev.* **2005**, *34*, 1048.

[56] S. A. Cotton, P. R. Raithby, *Coord. Chem. Rev.* **2017**, *340*, 220.

[57] K. Binnemans, *Chem. Rev.* **2009**, *109*, 4283.

[58] N. Lobanov, V. Smirnova, *Zh. Neorg. Khim.* **1963**, *8*, 2208.

[59] F. A. Hart, F. P. Laming, *J. Inorg. Nucl. Chem.* **1965**, *27*, 1825.

[60] S. Sinha, *Spectrochim. Acta* **1964**, *20*, 879.

[61] G. Novitskii, A. Borta, D. Ganzhu, S. Shova, I. G. Filippova, Y. A. Simonov, *Russ. J. Coord. Chem.* **2009**, *35*, 381.

[62] J. F. Bower, S. A. Cotton, J. Fawcett, R. S. Hughes, D. R. Russell, *Polyhedron* **2003**, *22*, 347.

[63] S. A. Cotton, O. E. Noy, F. Liesener, P. R. Raithby, *Inorg. Chim. Acta* **2003**, *344*, 37.

[64] D. Casanova, M. Llunell, P. Alemany, S. Alvarez, *Chem. Eur. J.* **2005**, *11*, 1479.

[65] Y. Zheng, J. Lin, Y. Liang, Y. Yu, Y. Zhou, C. Guo, S. Wang, H. Zhang, *J. Alloys Compd.* **2002**, *336*, 114.

[66] R. M. Ranson, E. Evangelou, C. B. Thomas, *Appl. Phys. Lett.* **1998**, *72*, 2663.

[67] Y. Liu, Y. Yang, G. D. Qian, Z. Y. Wang, M. Q. Wang, *Mat. Sci. Eng. B: Solid-State Mater. Adv. Technol.* **2007**, *137*, 74.

[68] S. Biju, D. B. A. Raj, M. L. P. Reddy, B. M. Kariuki, *Inorg. Chem.* **2006**, *45*, 10651.

[69] J. Shi, Y. Hou, W. Chu, X. Shi, H. Gu, B. Wang, Z. Sun, *Inorg. Chem.* **2013**, *52*, 5013.

[70] A. N. Carneiro Neto, E. E. S. Teotonio, G. F. de Sá, H. F. Brito, J. Legendziewicz, L. D. Carlos, M. C. F. C. Felinto, P. Gawryszewska, R. T. Moura, R. L. Longo, W. M. Faustino, O. L. Malta, in *Handbook on the Physics and Chemistry of Rare Earths*, Vol. 56 (Eds: J.-C. G. Bünzli, V. K. Pecharsky), Elsevier B.V., Amsterdam 2019, 55.

[71] Y. H. Pham, V. A. Trush, A. N. C. Neto, M. Korabik, J. Sokolnicki, M. Weselski, O. L. Malta, V. M. Amirkhanov, P. Gawryszewska, *J. Mater. Chem. C* **2020**, *8*, 9993.

[72] E. Kasprzycka, V. A. Trush, V. M. Amirkhanov, L. Jerzykiewicz, O. L. Malta, J. Legendziewicz, P. Gawryszewska, *Chem. Eur. J.* **2017**, *23*, 1318.

[73] C. R. S. Dean, R. S. Dean, T. M. Shepherd, *J. Chem. Soc. Faraday Trans. 2* **1975**, *71*, 146.

[74] M. J. Beltrán-Leiva, E. Solis-Céspedes, D. Páez-Hernández, *Dalton Trans.* **2020**, *49*, 7444.

[75] L. Wang, Q. Ou, Q. Peng, Z. Shuai, *J. Phys. Chem. A* **2021**, *125*, 1468.

[76] E. Hairer, G. Wanner, in *Encyclopedia of Applied and Computational Mathematics*, (Ed: B. Engquist), Springer Berlin Heidelberg, Berlin, Heidelberg 2015, 1213.

[77] B. R. Judd, *Phys. Rev.* **1962**, *127*, 750.

[78] G. S. Ofelt, *J. Chem. Phys.* **1962**, *37*, 511.

[79] O. L. Malta, *J. Lumin.* **1997**, *71*, 229.

[80] W. J. C. Grant, *Phys. Rev. B* **1971**, *4*, 648.

[81] M. Frisch, G. Trucks, H. Schlegel, G. Scuseria, M. Robb, J. Cheeseman, G. Scalmani, V. Barone, B. Mennucci, G. Petersson, in *Inc., Wallingford CT*, 2013.

[82] A. D. Becke, *J. Chem. Phys.* **1993**, *98*, 5648.

[83] C. Lee, W. Yang, R. G. Parr, *Phys. Rev. B* **1988**, *37*, 785.

[84] M. Dolg, H. Stoll, H. Preuss, *J. Chem. Phys.* **1989**, *90*, 1730.

[85] L. Smentek, A. Ke¸dziorski, **2010**, *130*, 1154.

[86] R. T. Moura, J. A. Oliveira, I. A. Santos, E. M. de Lima, L. D. Carlos, E. C. Aguiar, A. N. C. Neto, *Adv Theor Simul* **2021**, *4*.

[87] J. C. Wright, in *Radiationless Processes in Molecules and Condensed Phases: in Molecules and Condensed Phases*, Vol. 15 (Eds: D. J. Diestler, F. K. Fong, K. F. Freed, R. Kopelman, J. C. Wright), Springer Berlin Heidelberg, Berlin, Heidelberg 1976, 239.

## 9. Figures

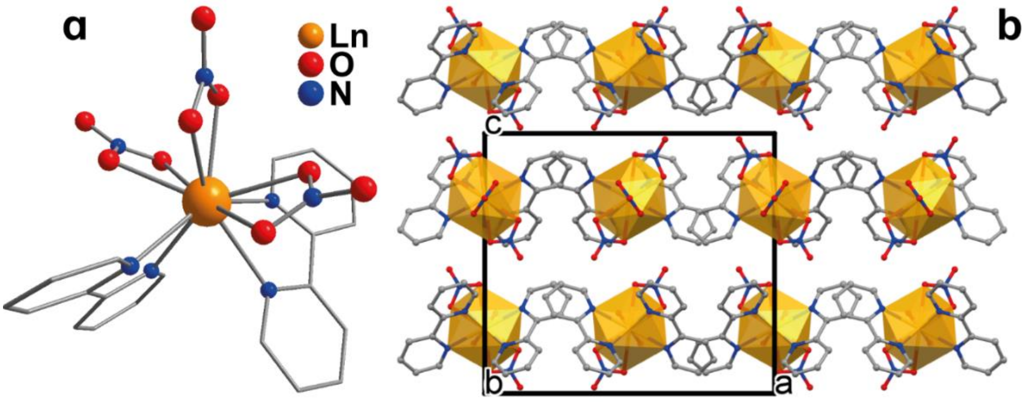

Figure 1. (a) Molecular structure of 1. (b) View of the crystal packing for 1 along the c crystallographic axis. Color code: orange, Eu/Tb; red, O; grey, C. Hydrogen atoms have been omitted for clarity.

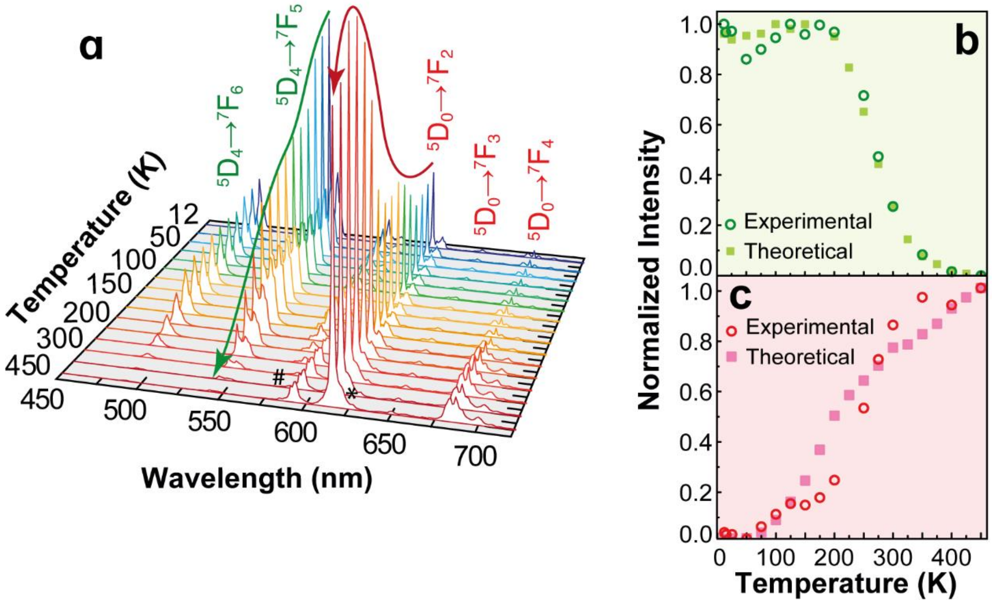

Figure 2. (a) Emission spectra of the complex 1 (11-450 K) excited at 330 nm. The spectra are normalized by the maximum intensity for each temperature value. The regions marked with * and # are superimposition between the $Eu^{3+}$ $^5D_0\rightarrow{}^7F_2$ and the $Tb^{3+}$ $^5D_4\rightarrow{}^7F_3$ and $Eu^{3+}$ $^5D_0\rightarrow{}^7F_{0,1}$ and the $Tb^{3+}$ $^5D_4\rightarrow{}^7F_4$, respectively. Experimental (circles) and theoretical values (squares) obtained for (b) $\boldsymbol{I_{Tb}}$ and (c) $\boldsymbol{I_{Eu}}$. The intensities $\boldsymbol{I_{Tb}}$ and $\boldsymbol{I_{Eu}}$ were normalized to the [0,1] range. The maximum uncertainty in the experimental values is $4\times10^{-4}$ (not visible in the presented scale).

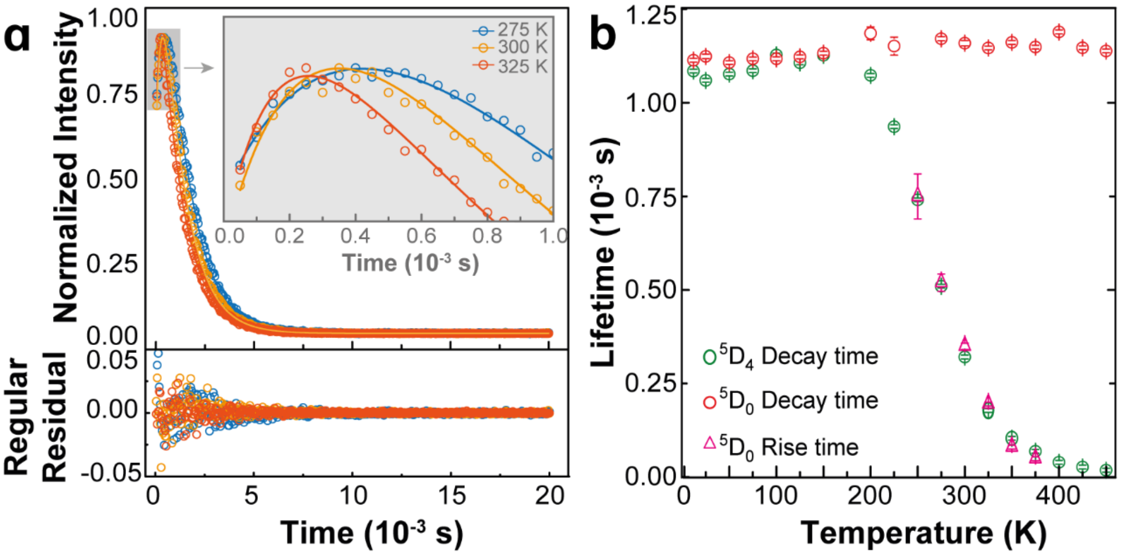

Figure 3. (a) $^5D_0$ emission decay curves acquired at 275, 300, and 325 K for 1 excited at 330 nm and monitored at 616 nm. The solid lines are the best fitting using Eq. 1. The regular residual plots are shown at the bottom. (b) $^5D_0$ and $^5D_4$ decay times and rise time of 1 recorded in 12-450 K range, excited at 330 nm and monitored at 542 and 616 nm, respectively.

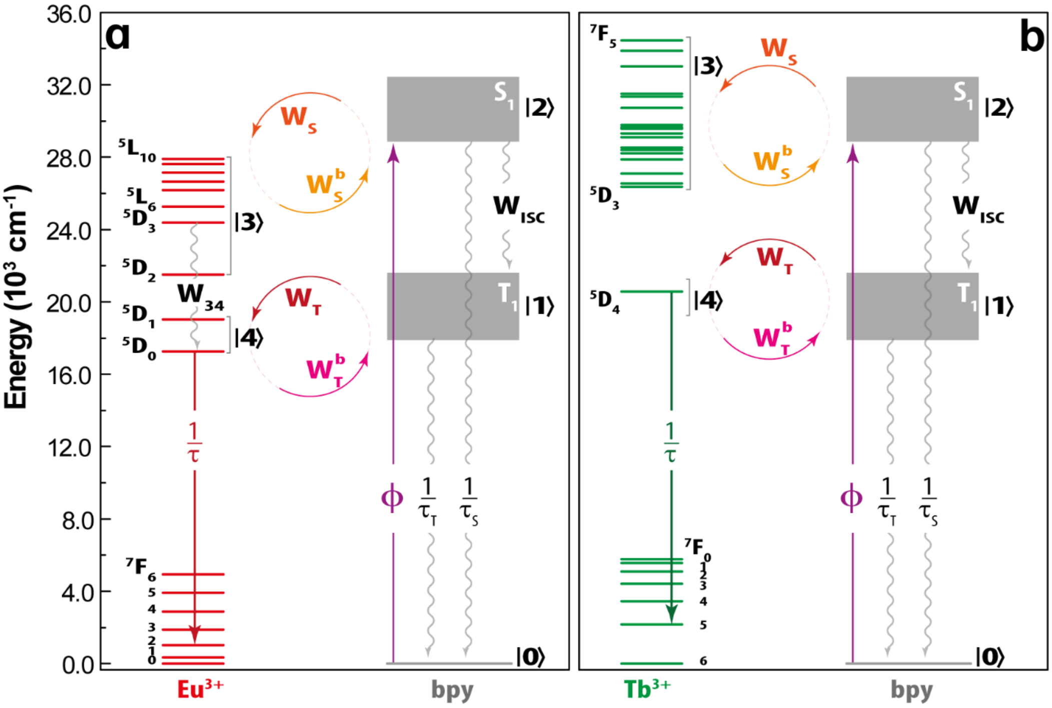

Figure 4. Energy level diagram for (a) Eu$^{3+}$ and (b) Tb$^{3+}$ in 1. $\boldsymbol{W_S}$ and $\boldsymbol{W_T}$ are the forward IET rates from the $S_1$ and $T_1$ states. Their respective backward IET rates are denoted with a superscript *b* ($\boldsymbol{W_S^b}$ and $\boldsymbol{W_T^b}$). $\boldsymbol{W_{ISC}}$ is the $S_1 \to T_1$ intersystem crossing rate, φ is the pumping rate, $\boldsymbol{W_{3\to4}}$ is the multiphonon relaxation rate from $|\mathbf{3}\rangle$ to $|\mathbf{4}\rangle$. The lifetimes $\boldsymbol{\tau_S}$, $\boldsymbol{\tau_T}$, and $\boldsymbol{\tau}$ are regarding the decay of $S_1$, $T_1$, and emitting levels ($^5D_0$ and $^5D_4$).

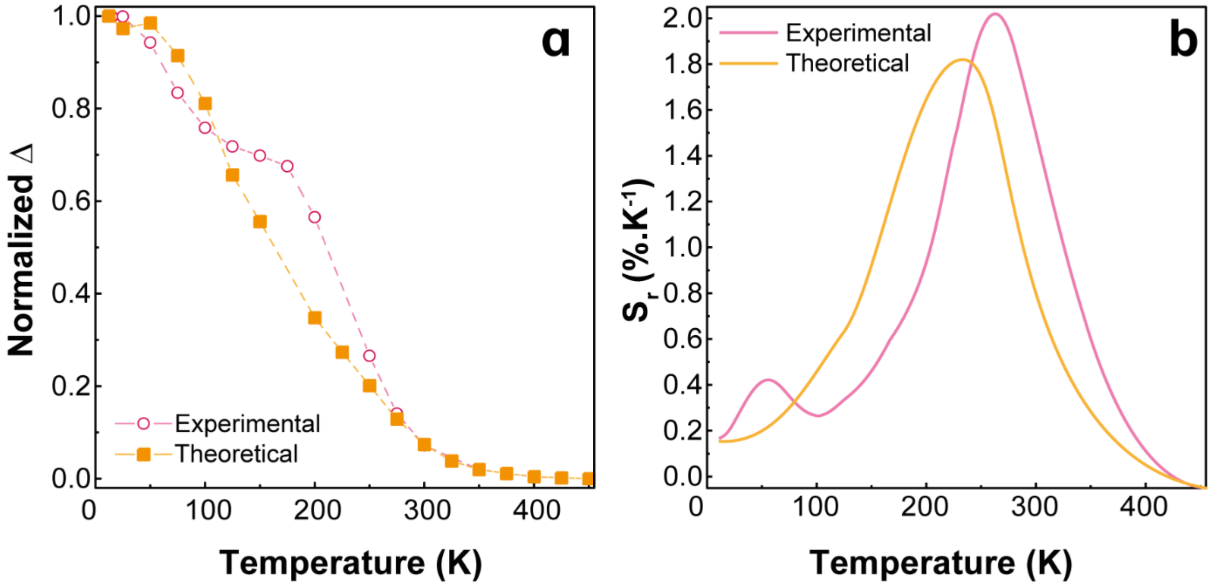

Figure 5. Temperature dependence of the (a) normalized thermometric parameters and (b) relative thermal sensitivity as a function of the temperature. The $S_r$ values were calculated using the numerical derivative of the points displayed in (a). The dashed lines are guides for the eyes.

## 10. Tables

Table 1. Calculated IET rates (in $s^{-1}$) as a function of the temperature for both complexes.

| | Eu$^{3+}$ complex | | | | Tb$^{3+}$ complex | | | |
|---|---|---|---|---|---|---|---|---|
| Temperature (K) | $\boldsymbol{W_T}$ ($10^6$) | $\boldsymbol{W_T^b}$ ($10^4$) | $\boldsymbol{W_S}$($10^4$) | $\boldsymbol{W_S^b}$ | $\boldsymbol{W_T}$($10^4$) | $\boldsymbol{W_T^b}$($10^6$) | $\boldsymbol{W_S}$($10^7$) | $\boldsymbol{W_S^b}$($10^4$) |
| 12 | 8.55 | 0.00228 | 1.61 | * | 7.04 | 4.18 | 1.82 | 1.06 |
| 25 | 8.55 | 0.00234 | 1.61 | * | 7.04 | 4.18 | 1.82 | 1.06 |
| 50 | 8.55 | 0.0532 | 1.87 | * | 7.04 | 4.18 | 1.82 | 1.06 |
| 75 | 8.52 | 0.620 | 4.03 | * | 7.04 | 4.18 | 1.82 | 1.07 |
| 100 | 8.47 | 2.38 | 8.94 | * | 7.04 | 4.18 | 1.82 | 1.08 |
| 125 | 8.39 | 5.53 | 15.9 | * | 7.04 | 4.18 | 1.82 | 1.10 |
| 150 | 8.29 | 9.86 | 23.8 | * | 7.04 | 4.18 | 1.82 | 1.12 |
| 200 | 8.10 | 20.6 | 40.3 | 0.000268 | 7.04 | 4.18 | 1.82 | 1.19 |
| 225 | 8.01 | 26.5 | 48.1 | 0.00164 | 7.04 | 4.18 | 1.82 | 1.22 |
| 250 | 7.92 | 32.4 | 55.5 | 0.00705 | 7.04 | 4.18 | 1.82 | 1.25 |
| 275 | 7.84 | 38.2 | 62.4 | 0.0238 | 7.04 | 4.18 | 1.82 | 1.28 |
| 300 | 7.76 | 43.8 | 68.9 | 0.0685 | 7.04 | 4.18 | 1.82 | 1.31 |
| 325 | 7.69 | 49.3 | 74.8 | 0.178 | 7.04 | 4.18 | 1.82 | 1.34 |
| 350 | 7.63 | 54.5 | 80.4 | 0.428 | 7.04 | 4.18 | 1.82 | 1.37 |
| 375 | 7.56 | 59.6 | 85.5 | 0.972 | 7.04 | 4.18 | 1.82 | 1.41 |
| 400 | 7.51 | 64.3 | 90.3 | 2.09 | 7.04 | 4.18 | 1.82 | 1.44 |
| 425 | 7.46 | 68.9 | 94.8 | 4.25 | 7.04 | 4.18 | 1.82 | 1.48 |
| 450 | 7.41 | 73.3 | 98.9 | 8.20 | 7.04 | 4.18 | 1.82 | 1.52 |

* values $<1\times10^{-5}$

Through a combined experimental and theoretical approach, we model the thermal properties of a luminescent Eu/Tb molecular thermometer in which the energy transfer drives the thermometric performance providing comprehensive guidelines, opening the avenue for the smart engineering of further dual center lanthanide-based thermal probes.

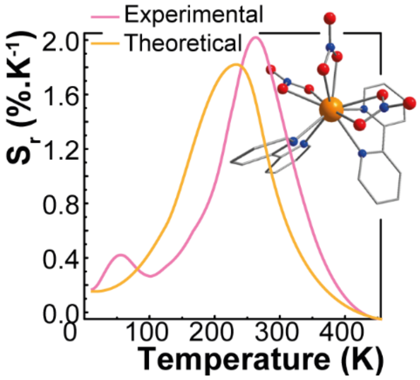

*Albano N. Carneiro Neto, Ekaterina Mamontova, Alexandre M. P. Botas, Carlos D. S. Brites Rute A. S. Ferreira, Jérôme Rouquette, Yannick Guari, Joulia Larionova, Jérôme Long, and Luís D. Carlos*

Rationalizing the thermal response of dual-center molecular thermometers: the example of an Eu/Tb coordination complex.